Bismuth Molybdate Nanoplates Supported on Reduced Graphene Oxide: An Effective Nanocomposite for the Removal of Naphthalene via Adsorption−Photodegradation

Shelter Maswanganyi, Rashi Gusain, Neeraj Kumar, Elvis Fosso-Kankeu,* Frans Boudewijn Waanders, and Suprakas Sinha Ray*

Read Online

ACCESS | Metrics & More | Article Recommendations

ABSTRACT: Polycyclic aromatic hydrocarbons are a class of persistent organic water pollutants that raise serious concerns owing to their carcinogenicity and other negative impacts on humans and ecosystems. In this study, Bi_2MoO_6/reduced graphene oxide (rGO) nanocomposites were designed and prepared for the adsorption-assisted photodegradation of naphthalene molecules in an aqueous medium. The synthesized Bi_2MoO_6 nanoplates and Bi_2MoO_6/rGO nanocomposites were characterized by X-ray diffraction, Fourier transform infrared, scanning electron microscopy, high-resolution transmission microscopy, X-ray photoelectron spectroscopy, ultraviolet spectroscopy, Brunauer−Emmett−Teller, and photoluminescence measurements. The photodegradation of naphthalene molecules was observed to assess the photocatalytic characteristics of the samples under visible light. The Bi_2MoO_6/rGO nanocomposites exhibited significantly improved photocatalytic efficiency compared to pure Bi_2MoO_6. Among the nanocomposites, those containing 2 wt % rGO showed the best photocatalytic activity. The incorporation of rGO enhanced the visible light absorption and decreased the recombination rate of photogenerated charge carriers. Moreover, a Bi_2MoO_6/rGO nanocomposite showed excellent reusability for five cycles.
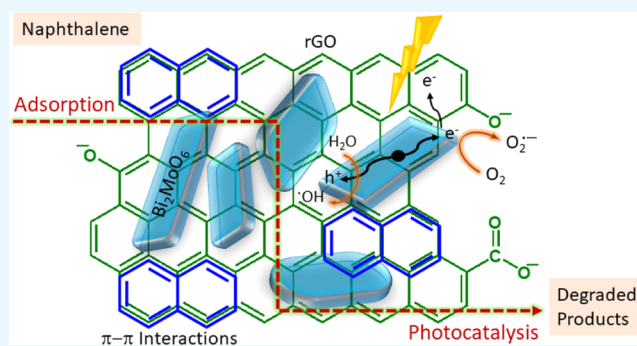
1. INTRODUCTION

Water pollution remains a global challenge that cannot be eliminated because the majority of water pollutants come from anthropogenic activities that are crucial to human life. These activities may release water effluents containing contaminants that include heavy metals, pesticides, chemical waste, hydrocarbons, and persistent organic pollutants.[1−5] Persistent organic pollutants, in particular polycyclic aromatic hydrocarbons (PAHs), attract considerable attention in water pollution studies owing to their toxic, mutagenic, and carcinogenic potential.[6,7] PAHs are a group of organic compounds consisting of two or more benzene rings attached in a clustered, linear, or angular arrangement. Approximately 16 PAHs in the environment are listed as priority contaminants by the US Environmental Protection Agency.[7] Most hazardous PAHs in the environment originate from industry (coke production, sewage sludge, organic waste, etc.), domestic heating (the burning of coal, wood, gas; incomplete combustion of fossil fuels; cigarettes; etc.), agricultural sources (pesticides), and natural sources (volcanic eruptions, the decay of organic matter, forest fires, etc.).[7,8] PAHs from industrial processes can enter water bodies through leachates from dumpsites, coal mines, and steel-making plants.[9]

Continuous exposure to environmental PAHs has detrimental impacts on flora and fauna. Humans are exposed to PAHs through breathing, drinking, dermal contact, and the ingestion of food grown in PAH-contaminated soil.[10] Additionally, regular exposure to PAHs can have various health effects in humans, including skin irritation, diarrhea, breathing problems, and skin and lung cancer.[7] Owing to the negative health impacts, effective methods for the removal of PAHs from water have been extensively investigated. PAHs can be removed from the aquatic environment using various techniques, such as physical, chemical, and biological methods.[3,11−14] According to previous studies, physical and biological processes can remove PAHs from water; however, they are inefficient, as they cannot completely remove or degrade PAHs, which remain in the environment as secondary
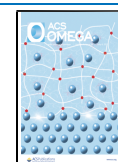
generated waste. Owing to challenges such as the toxicity, complexity, and costs associated with the use of physical and biological methods, chemical wastewater treatment methods such as photocatalysis, the use of Fenton's reagent, peroxonation, and ozonation have been widely used as alternatives for removing PAHs from the aquatic environment.[15−17] Among chemical methods, photocatalytic degradation has been widely investigated because it is clean, cost-effective, simple, and more efficient.

Several organic and inorganic materials have been used as photocatalysts for PAH degradation.[18,19] Bismuth-based semiconductor materials have been extensively studied recently for use as photocatalysts owing to their high light-harvesting efficiency, corrosion resistance, low cost, ability to respond to UV and visible light, chemical inertness, nontoxicity, and catalytic properties.[20,21] Among many bismuth-based photocatalysts, bismuth molybdate (Bi_2MoO_6) is a suitable semiconductor material for water contaminant degradation under visible light irradiation owing to its narrow band gap (∼2.7 eV).[22−24] However, the fast recombination of photogenerated charge carriers (i.e., electron−hole pairs) reduces the usefulness of Bi_2MoO_6 photocatalysts. To further improve the photocatalytic performance of Bi_2MoO_6 and address this limitation, Bi_2MoO_6 is usually supported by organic or inorganic materials to suppress the electron−hole recombination. Among two-dimensional organic supports, reduced graphene oxide (rGO) has typically been employed owing to its unique properties such as excellent conductivity, a high surface-to-volume ratio, and high catalytic and mechanical properties.[25−27] Bi_2MoO_6/rGO composites have demonstrated improved photocatalytic activity for hydrogen production,[28] CO_2 reduction,[29] and dye degradation[30,31] owing to the presence of electron-rich interfaces and high electron extraction and transport at the synergistic interface between Bi_2MoO_6 and rGO.

In this study, Bi_2MoO_6 nanoplates were grown over different amounts of rGO by a hydrothermal method to form Bi_2MoO_6/rGO nanocomposites; their photocatalytic performance in the degradation of naphthalene in simulated wastewater was examined. The effects of factors such as reaction time, dopant concentration, and pollutant concentration in the water was used to assess the efficiency of the prepared catalyst. To examine the PAH degradation efficiency of the Bi_2MoO_6/rGO nanocomposites, naphthalene was used as a representative PAH water-contaminant model. The photodegradation of naphthalene by pure Bi_2MoO_6 and the Bi_2MoO_6/rGO nanocomposites was then compared.

2. RESULTS AND DISCUSSION

Bi_2MoO_6 was synthesized by a hydrothermal method at 180 °C without using an acid or a surfactant. To obtain the Bi_2MoO_6/rGO nanocomposites, Bi_2MoO_6 was prepared with different amounts of graphene oxide (GO). GO was hydrothermally converted to rGO in situ at 180 °C to produce Bi_2MoO_6/rGO nanocomposites.[32]

2.1. Structural and Morphological Characterization.
Figure 1 shows the X-ray diffraction (XRD) patterns of the prepared pure Bi_2MoO_6 and Bi_2MoO_6/rGO nanocomposite materials. The XRD peaks of pure Bi_2MoO_6 and the Bi_2MoO_6/rGO nanocomposites do not differ significantly. The rGO peaks were not detected in the XRD patterns of Bi_2MoO_6/rGO, possibly owing to the high crystallinity and strong diffraction pattern of Bi_2MoO_6 and the low rGO concen-
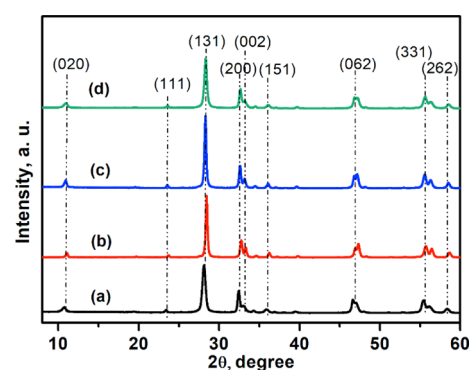
Figure 1. XRD patterns of (a) Bi_2MoO_6, (b) Bi_2MoO_6/rGO (2 wt % rGO), (c) Bi_2MoO_6/rGO (5 wt % rGO), and (d) Bi_2MoO_6/rGO (10 wt % rGO).

tration. The sharp intense XRD peaks indicate that the samples have a high degree of crystallinity. All the as-prepared samples show the characteristic peaks of the (020), (111), (131), (200), (002), (151), (062), (331), and (262) planes at $2\theta =$ 10.98, 23.54, 28.31, 32.17, 33.16, 35.96, 46.97, 55.87, and 88.36°, respectively. These diffraction peaks can be assigned to the pure orthorhombic phase of Bi_2MoO_6 according to the standard card JCPDS no. 76-238.[33] Moreover, the absence of any other phase in the XRD patterns indicates that the Bi_2MoO_6/rGO nanocomposites have high purity.

Fourier transform infrared (FTIR) analysis was performed to identify the surface functional group of the materials. Figure 2
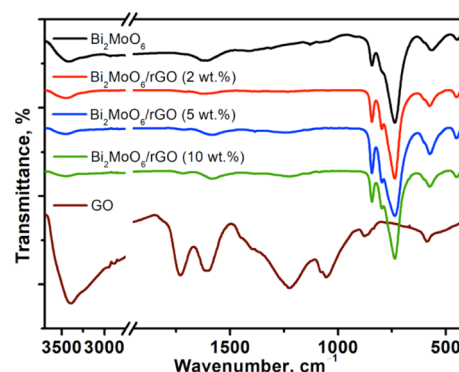
Figure 2. FTIR spectra of Bi_2MoO_6 nanoplates, GO, and Bi_2MoO_6/rGO (2, 5, and 10 wt % rGO) nanocomposites.

shows the FTIR spectra of the prepared Bi_2MoO_6/rGO nanocomposites, pure Bi_2MoO_6, and GO. The main absorption peaks of the pure Bi_2MoO_6 and Bi_2MoO_6/rGO nanocomposites at 400−850 cm^{-1} are attributed to the Mo−O and Bi−O stretching and Mo−O−Mo bridging stretching modes in the Bi_2MoO_6 crystal structure.[33] Strong peaks in this range are observed at wavenumbers of approximately 837 and 797 cm^{-1} and are ascribed to the asymmetric and symmetric stretching modes of MoO_6 that involve the vibration of apical oxygen atoms, respectively.[34] However, the vibrational signature at 734 cm^{-1} can be assigned to the asymmetric stretching of MoO_6 associated with the vibration of equatorial oxygen.[35] The vibrational band at 446 cm^{-1} can be attributed to the bending and stretching vibration of octahedral BiO_6.[36]

The standard GO spectrum exhibits relatively small absorbance bands at wavenumbers of 3500−1000 cm^{-1}, which are attributed to representative oxygen functional

groups. The absorbance bands identified in the GO spectrum are due to O−H stretching (3394 cm^{-1}), C=O (1724 cm^{-1}), C=C bending (1604 cm^{-1}), C−OH (1215 cm^{-1}), and C−O (1047 cm^{-1}).[37,38] Another peak at 590 cm^{-1} is ascribed to the O−H out-of-plane band. However, some of these peaks do not appear in the Bi$_2$MoO$_6$/rGO FTIR spectrum or their intensity is significantly decreased, which confirms that GO is reduced to rGO during the preparation of the nanocomposite. The low-intensity peaks at 3450, 1726, 1584, and 1234 cm^{-1} can be ascribed to −OH, −C=O, C=C, and −C−OH functional groups, respectively.

The surface morphologies of pure Bi$_2$MoO$_6$ and the Bi$_2$MoO$_6$/rGO (2 wt % rGO) nanocomposite were examined by field emission scanning electron microscopy (FESEM) analysis. The FESEM images in Figure 3a clearly show the
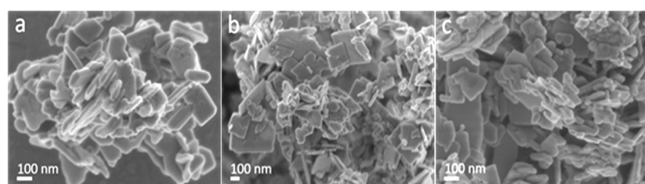
Figure 3. FESEM images of (a) Bi$_2$MoO$_6$ nanoplates and (b) Bi$_2$MoO$_6$/rGO (2 wt %) nanocomposite (b,c) at different magnifications.

formation of irregular nanoplates with a structure resembling that of pure Bi$_2$MoO$_6$. Figure 3b,c shows FESEM images of the Bi$_2$MoO$_6$/rGO (2 wt % rGO) nanocomposite, which show a hybrid nanostructured material composed of irregular nanoplates. This result indicates that the incorporation of rGO into Bi$_2$MoO$_6$ particles strongly affects the surface morphology of Bi$_2$MoO$_6$. The FESEM images of the Bi$_2$MoO$_6$/rGO (2 wt % rGO) nanocomposite also demonstrate a strong interaction between the rGO nanosheets and Bi$_2$MoO$_6$ nanoplates, as they show that almost all of the Bi$_2$MoO$_6$ particles were well embedded in the rGO thin nanosheets. Discrete rGO sheets are not visible in the FESEM images of the nanocomposite owing to the very low rGO concentration, and most of the rGO sheet is covered by perfect Bi$_2$MoO$_6$ nanoplates.

The Bi$_2$MoO$_6$/rGO (2 wt % rGO) nanocomposite was further investigated by high-resolution transmission electron microscopy (HRTEM), which reveals the internal structure of the synthesized monohybrid material. Figure 4a shows a high-resolution morphological image of GO thin sheets with a multilayer structure. Figure 4b,d shows high-resolution morphological images of flat irregular nanoplates of pure Bi$_2$MoO$_6$. The lattice fringe d-spacing of 0.319 in Figure 4c,d corresponds to the (111) plane of orthorhombic Bi$_2$MoO$_6$. Figure 4e,f shows the interfacial cross-mixing structure of the rGO nanosheets and Bi$_2$MoO$_6$ nanostructured material. Figure 4g reveals an interlayer spacing of 0.36 nm in the rGO nanosheets, which is characteristic of the (002) plane of few-layer rGO.

The Bi$_2$MoO$_6$/rGO (2 wt % rGO) nanocomposite was also analyzed using scanning tunneling electron microscopy (STEM) and elemental mapping to identify the composition of the material. Figure 5a clearly shows Bi$_2$MoO$_6$ particles covered by a thin transparent sheet of rGO. Elemental mapping images reveal the elemental composition of the Bi$_2$MoO$_6$/rGO nanocomposite. A strong carbon peak (Figure 5b) in the energy-dispersive X-ray (EDX) spectrum shows that
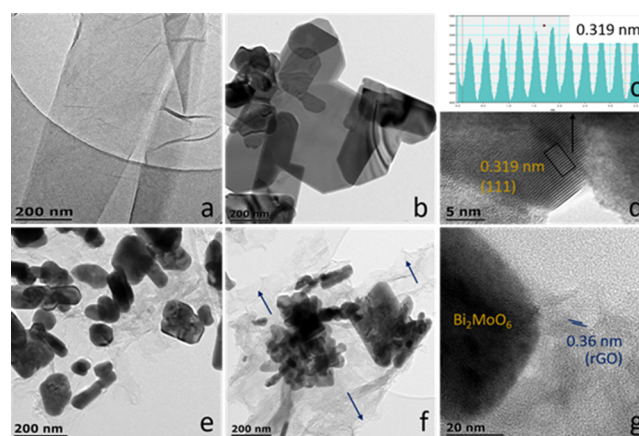
Figure 4. HRTEM images of (a) GO, (b,d) Bi$_2$MoO$_6$ nanoplates, (c) d-spacing calculation using the average of 10 fringes in a particular area in (d), and (e−g) Bi$_2$MoO$_6$/rGO (2 wt % rGO) nanocomposite.

the rGO nanosheet has a high carbon content. The spectrum also reveals the presence of Bi, Mo, and O in Bi$_2$MoO$_6$, which are uniformly distributed on the rGO sheet. Strong Bi and Mo peaks appear at approximately 2.5 keV, and oxygen peaks appear at approximately 0.5 keV. No elements other than those constituting the Bi$_2$MoO$_6$/rGO nanocomposite appear in the spectrum of the prepared catalyst. Thus, a high-purity Bi$_2$MoO$_6$/rGO nanocomposite was successfully synthesized. The strong copper peak in the spectrum results from the copper used in the analytical procedure (TEM grid).

X-ray photoelectron spectroscopy (XPS) was used to analyze the surface composition and elemental chemical states of the Bi$_2$MoO$_6$/rGO nanocomposite. Figure 6a shows the survey spectra of the Bi$_2$MoO$_6$/rGO (2 wt % rGO) nanocomposite and pure Bi$_2$MoO$_6$, which exhibit characteristic O 1s, C 1s, Mo 3d, and Bi 4f peaks, with no impurities. In addition, the spectrum of the Bi$_2$MoO$_6$/rGO (2 wt % rGO) nanocomposite shows a much stronger C 1s peak than that of pure Bi$_2$MoO$_6$, which indicates a relatively high concentration of C owing to the presence of rGO. Figure 6b shows the high-resolution C 1s spectrum, which exhibits four peaks at 284.7, 286.2, 287.5, and 288.7 eV. The peaks at 284.7 and 286.2 eV are associated with the sp^2 carbon (C=C) and sp^3 carbon (C−C/C−O−C/C−OH) in the material, respectively.[39] The peaks at 287.5 and 288.7 eV are ascribed to carbonyl carbons (C=O) and COOH, respectively. The O 1s XPS spectra of pure Bi$_2$MoO$_6$ (Figure 6c) show three distinct peaks at 529.8, 530.0, and 531.7 eV, which can be indexed to Mo−O, Bi−O, and surface hydroxyl groups, respectively.[40] However, the O 1s spectrum of Bi$_2$MoO$_6$/rGO shows four distinct peaks, where the high-intensity peak at 531.7 eV and the peak at 533 eV are attributed to the C−O and C=O functional groups, respectively. The high-resolution Bi 4f XPS spectrum (Figure 6d) consists of only two peaks with binding energies of 158.8 and 164.1 eV, which are ascribed to Bi 4f$^{7/2}$ and Bi 4f$^{5/2}$, respectively, demonstrating that the Bi in Bi$_2$MoO$_6$ is in the Bi^{3+} oxidation state.[41] Furthermore, the Mo 3d spectrum in Figure 6e shows two peaks at 232.1 and 235.2 eV, which are attributed to Mo 3d$^{5/2}$ and Mo 3d$^{3/2}$, respectively, and indicate that Mo is present in the Mo^{6+} oxidation state.[42] The XPS analysis confirms that the Bi$_2$MoO$_6$/rGO (2 wt % rGO) photocatalyst was successfully synthesized.

The optical properties of pure Bi$_2$MoO$_6$ and Bi$_2$MoO$_6$/rGO nanocomposite samples were studied using the UV−visible
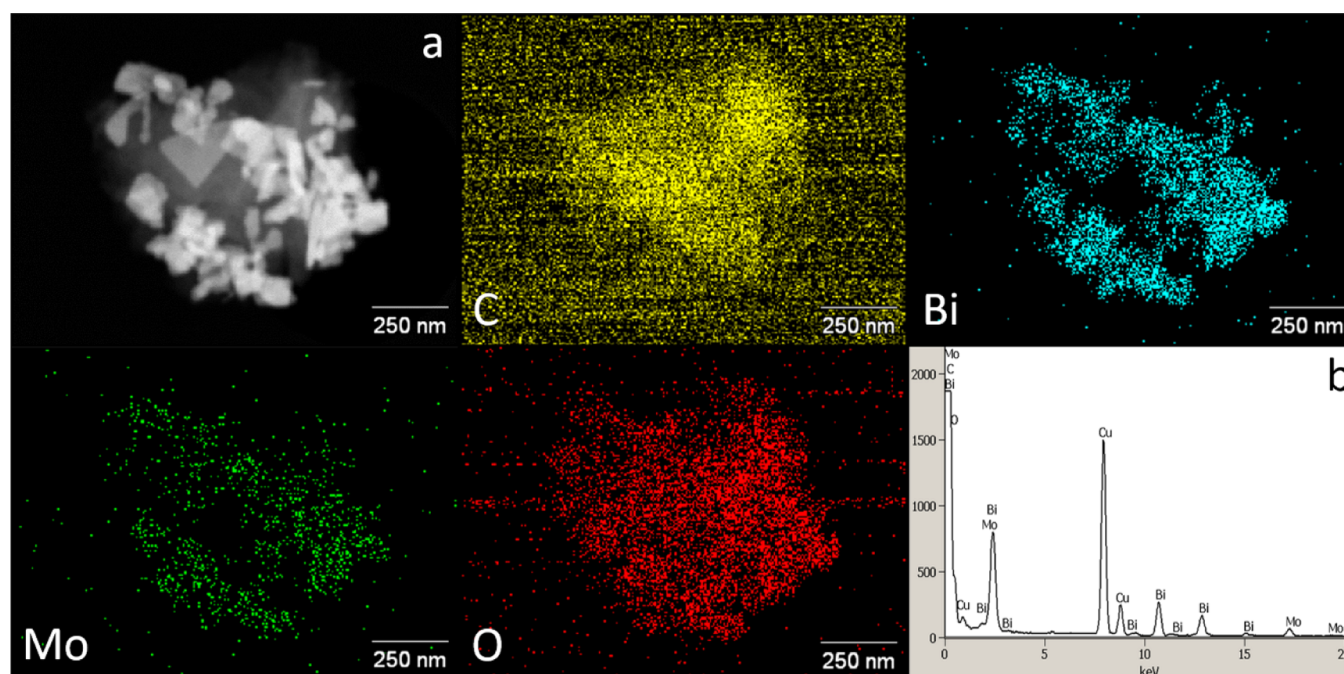
Figure 5. (a) STEM image and EDX mapping images, which show homogeneous distributions of C, Bi, Mo, and O, and (b) EDX spectrum of the Bi_2MoO_6/rGO (2 wt % rGO) nanocomposite.
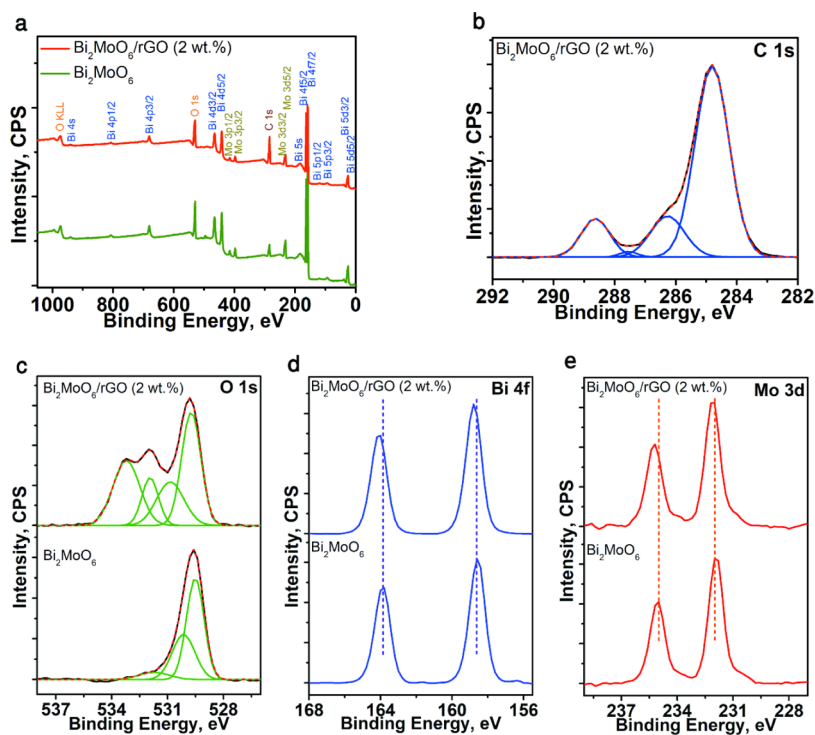
Figure 6. (a) XPS survey spectra of Bi_2MoO_6 and the Bi_2MoO_6/rGO (2 wt % rGO) nanocomposite. High-resolution XPS binding energy spectra: (b) C 1s, (c) O 1s, (d) Bi 4f, and (e) Mo 3d.

(UV−vis) absorbance spectra. Figure 7a displays the UV−vis absorbance patterns of all the prepared samples. Pure Bi_2MoO_6 shows a typical UV−vis absorbance spectrum with a steep edge near 430 nm. All of the Bi_2MoO_6/rGO nanocomposite materials exhibit enhanced absorbance in the visible region compared to pure Bi_2MoO_6. The spectral observations reveal that the wavelength range of the visible light response of Bi_2MoO_6 is broader in the presence of rGO, which is crucial to

the enhancement of its photocatalytic properties under solar irradiation. The broadening of the visible light response can be attributed to the presence of black rGO particles, which increase the surface electric charge of the Bi_2MoO_6/rGO nanocomposites and further support the electron−hole pair formation process during photocatalysis. In addition, the reduced oxygen functional groups and an increase in aromatic rings in rGO facilitate easy electron excitation at a lower
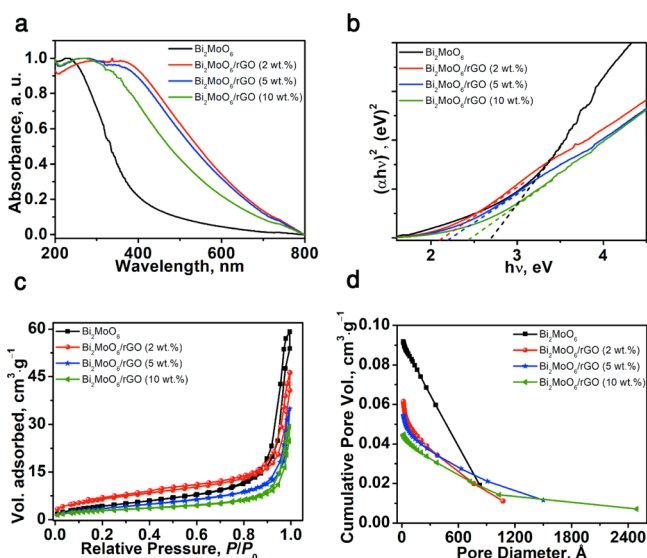
Figure 7. (a) UV−vis absorbance spectra, (b) Tauc plots for band gap calculation, (c) N$_2$ adsorption−desorption isotherms, and (d) pore size distribution of Bi$_2$MoO$_6$ and Bi$_2$MoO$_6$/rGO (0, 2, 5, and 10 wt % rGO) nanocomposites.

energy. These results confirm that the addition of GO to Bi$_2$MoO$_6$ significantly improves the visible light response. The band gaps of the samples were also estimated using the Tauc plots, as shown in Figure 7b. The plot was obtained by drawing a graph of $(\alpha h\nu)^2$ versus $(h\nu)$ as follows

$$\alpha h\nu = A(h\nu - E_g)^{n/2} \qquad (1)$$

where A, E_g, ν, h, and α are a constant, the band gap, the optical frequency, the Planck constant, and the absorption coefficient, respectively; n was assumed to be 4.[30] The band gaps estimated from the Tauc plot were 2.7, 2.1, 2.2, and 2.45 eV for pure Bi$_2$MoO$_6$ and the Bi$_2$MoO$_6$/rGO (2 wt % rGO), Bi$_2$MoO$_6$/rGO (5 wt % rGO), and Bi$_2$MoO$_6$/rGO (10 wt % rGO) nanocomposites, respectively. All the Bi$_2$MoO$_6$/rGO nanocomposites have smaller band gaps than pure Bi$_2$MoO$_6$, possibly because of interactions between the unpaired π-electrons of rGO and electrons on the surface of Bi$_2$MoO$_6$.[43] The smaller band gap is a promising characteristic suggesting an enhanced photocatalytic activity. The band gap increases slightly with increasing rGO content, possibly owing to the aggregation of the rGO nanosheets.

Figure 7c shows the nitrogen adsorption−desorption isotherms of pure Bi$_2$MoO$_6$ and Bi$_2$MoO$_6$/rGO nano-composite samples. The isotherm curves of the Bi$_2$MoO$_6$/rGO nanocomposite samples and pure Bi$_2$MoO$_6$ are the same, and they are classified as type IV. Materials in the type IV class exhibit a hysteresis loop and mesoporous structure.[44] The Brunauer−Emmett−Teller surface area of the Bi$_2$MoO$_6$/rGO (2 wt % rGO) nanocomposite (24 m^2·g^{-1}) was higher than those of pure Bi$_2$MoO$_6$ (17 m^2·g^{-1}) and the Bi$_2$MoO$_6$/rGO (5 wt % rGO) (14 m^2·g^{-1}) and Bi$_2$MoO$_6$/rGO (10 wt % rGO) (10 m^2·g^{-1}) nanocomposites. The high surface area of the Bi$_2$MoO$_6$/rGO (2 wt % rGO) nanocomposite provides more surface active sites, which support the photocatalytic activity of the photocatalyst. The pore size distribution of the synthesized samples (Figure 7d) was measured using the Barrett−Joyner−Halenda method and is summarized in Table 1. The

incorporation of GO into Bi$_2$MoO$_6$ reduced the pore size of the nanocomposite materials.

Table 1. Effect of the rGO Content on the Surface Area and Porosity of Bi$_2$MoO$_6$

material	specific surface area (m^2·g^{-1})	average pore volume (cm^3·g^{-1})	average pore diameter (Å)
Bi$_2$MoO$_6$	17	0.092	105.16
Bi$_2$MoO$_6$/rGO (2 wt % rGO)	24	0.066	54.94
Bi$_2$MoO$_6$/rGO (5 wt % rGO)	14	0.054	67.07
Bi$_2$MoO$_6$/rGO (10 wt % rGO)	10	0.045	69.54

2.2. Removal of Naphthalene via Adsorption−Photo-degradation. *2.2.1. Adsorption Studies.* Figure 8a presents the effect of contact time on the adsorption efficiency of the Bi$_2$MoO$_6$/rGO (2 wt % rGO) nanocomposite. The adsorption of naphthalene by the Bi$_2$MoO$_6$/rGO nanocomposite is very rapid; within 5 min, more than 50% of the naphthalene was adsorbed, and naphthalene molecules were continuously adsorbed on the photocatalyst surface as the reaction progressed until the adsorption−desorption equilibrium was reached. After 60 min, at least 80% of the naphthalene was adsorbed. After 60 min, the adsorption−desorption equilibrium was established between the adsorbate and adsorbent. Therefore, it can be concluded that 60 min is the most effective time for naphthalene adsorption using the Bi$_2$MoO$_6$/rGO nanocomposite, and this time was used in the rest of the study. The effect of the rGO content of the Bi$_2$MoO$_6$ particles on the adsorption efficiency was also investigated, as shown in Figure 8b. The efficiency of the Bi$_2$MoO$_6$/rGO (0, 5, and 10 wt % rGO) nanocomposites clearly exhibits the same overall behavior as that of the Bi$_2$MoO$_6$/rGO (2 wt % rGO) nanocomposite.

However, the adsorption rates of the synthesized materials differ. Among them, Bi$_2$MoO$_6$/rGO (2 wt % rGO) shows the highest adsorption efficiency for naphthalene, which might be attributable to the fact that it has the highest active surface area. Therefore, the Bi$_2$MoO$_6$/rGO (2 wt % rGO) nano-composite was chosen as the model adsorbent/photocatalyst for the rest of the study. Owing to the rGO skeleton in the Bi$_2$MoO$_6$/rGO nanocomposites, all the nanocomposites show higher adsorption efficiency for naphthalene than pure Bi$_2$MoO$_6$. The rGO in the nanocomposite material is enriched in π-electrons, which facilitate naphthalene adsorption via $\pi-\pi$ interactions with aromatic naphthalene.[45] In addition, the adsorption efficiency of the nanocomposites decreases with increasing rGO content. The reason might be that the specific surface area decreases with increasing rGO content, which decreases the number of active sites for naphthalene adsorption. The continuous increase in the adsorption efficiency of all the nanocomposites with increasing contact time is due to the occupation of some of the active sites of the adsorbent by contaminants, which increases with time.

The effect of the initial concentration on the adsorption of naphthalene by the Bi$_2$MoO$_6$/rGO (2 wt % rGO) nano-composite was analyzed by varying the initial concentration of the naphthalene solution (25, 50, 75, and 100 ppm). Figure 9a reveals that with the increasing initial concentration of the contaminant, the removal efficiency of the adsorbent decreases. The reason is that although the number of contaminant
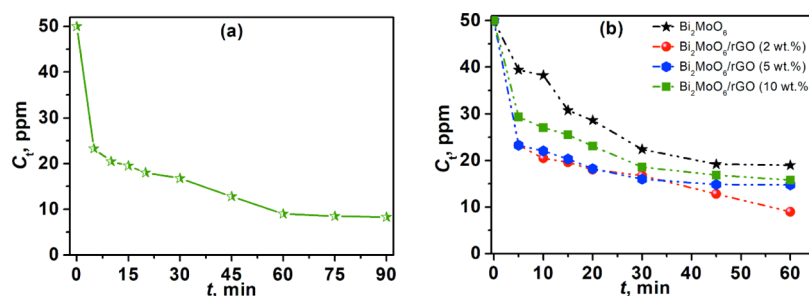
Figure 8. (a) Effect of contact time on naphthalene adsorption using Bi_2MoO_6/rGO (2 wt % rGO). (b) Effect of the rGO content of Bi_2MoO_6/rGO nanocomposites on the removal of naphthalene from wastewater. Conditions: 30 mg of adsorbent (Bi_2MoO_6/rGO), 100 mL of 50 ppm naphthalene solution, 25 °C, and 60 min.
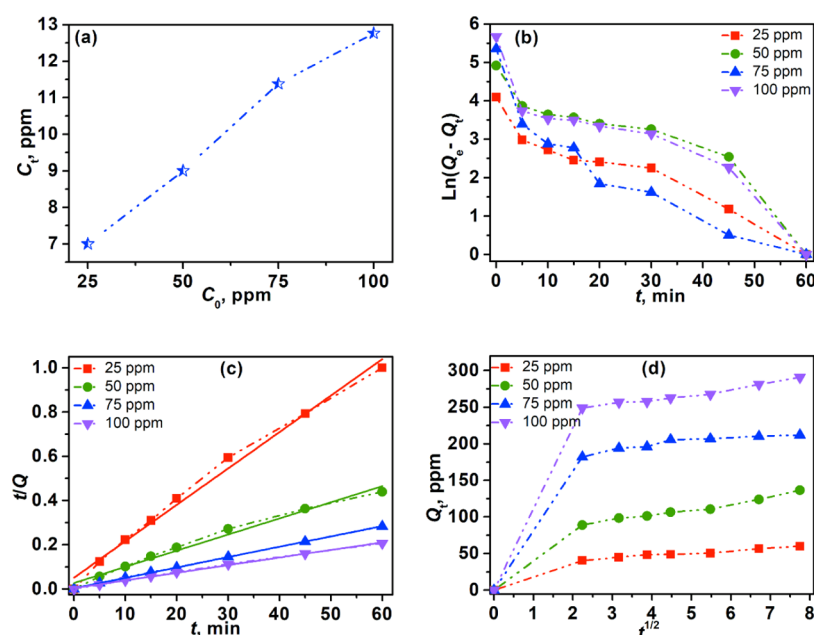
Figure 9. (a) Effect of the initial naphthalene concentration on the removal efficiency of the Bi_2MoO_6/rGO (2 wt % rGO) nanocomposite, (b) pseudo-first-order and (c) pseudo-second-order adsorption kinetics, and (d) intraparticle diffusion kinetics of naphthalene adsorption using the Bi_2MoO_6/rGO (2 wt % rGO) nanocomposite. Conditions: 30 mg of adsorbent [Bi_2MoO_6/rGO (2 wt %) nanocomposite], 100 mL of naphthalene solutions of 25, 50, 75, and 100 ppm, 25 °C, and 60 min.

molecules increases, the number of active adsorption sites on the adsorbent is constant. Therefore, owing to the limited number of available active sites for naphthalene adsorption on the adsorbent, the removal efficiency decreases with increasing naphthalene content.

The naphthalene adsorption kinetics was studied to clarify the adsorption mechanism of the Bi_2MoO_6/rGO nanocomposite for naphthalene removal in water. The pseudo-first-order, pseudo-second-order, and intraparticle diffusion kinetic models were used to investigate the adsorption mechanism. The kinetic study also helped to determine and express the rates of the determining steps for pollutant removal from aqueous solution. The linear pseudo-first-order kinetics is defined as

$$\ln(Q_e - Q_t) = \ln Q_e - k_1 t \tag{2}$$

Here, Q_t and Q_e represent the mass of adsorbed naphthalene molecules (mg) per gram of adsorbent at time t (min) and at equilibrium, respectively, and k_1 is the pseudo-first-order rate constant (min^{-1}). The values of k_1 and Q_e can be obtained

from the slope and intercept of the linear plot of $\ln(Q_e - Q_t)$ versus t (Figure 9b). Q_t can be calculated as follows

$$Q_t = (C_o - C_t) \cdot \frac{V}{m} \tag{3}$$

Here, C_o and C_t are the initial naphthalene concentration (mg) and the concentration after time t (min) in the solution, V is the volume of the solution (mL), and m is the weight of the adsorbent (mg).

R^2 (the coefficient of determination) is calculated from the linear graph and is used to identify the kinetic model that best fits the adsorption process. The highest R^2 value indicates the best-fitted model. The graph plotted for the pseudo-first-order kinetics from the experimental values shows a low R^2 value and does not yield a linear relationship (Figure 9b). This result implies that the pseudo-first-order model does not describe the naphthalene adsorption mechanism of the Bi_2MoO_6/rGO nanocomposite.

The pseudo-second-order kinetic model was also studied to determine whether it is applicable to the naphthalene adsorption process. The pseudo-second-order equation is given as

$$\frac{t}{Q_t} = \frac{1}{k_2 Q_e^2} + \frac{t}{Q_e} \qquad (4)$$

Here, k_2 is the pseudo-second-order rate constant ($\text{g}\cdot\text{mg}^{-1}\cdot\text{min}^{-1}$). Figure 9c presents the pseudo-second-order kinetics, specifically, a plot of t/Q_t versus t. The kinetic parameters for the pseudo-second-order model were estimated using the slope and intercept of the graph in Figure 9c. The calculated values were found to be very similar to the experimental values, as shown in Table 2. Furthermore, Figure 9c indicates a linear

Table 2. Pseudo-Second-Order Kinetic Parameters for Naphthalene Adsorption by Bi_2MoO_6/rGO (2 wt %)

initial naphthalene concentration, $\text{mg}\cdot\text{L}^{-1}$	pseudo-second-order kinetic parameters			
	$Q_{e,\text{cal}}$	$Q_{e,\text{exp}}$	$k_2 \times 10^{-4}$, ($\text{g}\cdot\text{mg}\cdot\text{min}^{-1}$)	R^2
25	60	60.75	2.95	0.99
50	133.33	137.174	2.82	0.98
75	212.066	214.13	2.49	0.99
100	290.78	291.54	2.2	0.99

relationship and a high R^2 value, indicating that the pseudo-second-order model can be used to describe the naphthalene adsorption mechanism. Figure 9d shows the intraparticle diffusion model of naphthalene adsorption. The linear intraparticle diffusion kinetic model is expressed as

$$Q_t = k_{id} t^{1/2} + C \qquad (5)$$

Here, k_{id} is the intraparticle diffusion constant ($\text{mg}\cdot\text{g}^{-1}\cdot\text{min}^{-1/2}$). The plot of Q_t versus $t^{1/2}$ also does not show a linear relationship between the two variables and yields a low R^2 value. This result confirms that the model is not applicable to naphthalene adsorption, and intraparticle diffusion cannot be the rate-determining step.

Adsorption isotherm studies were conducted to analyze the relationship between the amount of naphthalene adsorbed on the photocatalyst surface and the naphthalene concentration in the solution at equilibrium. This relationship was analyzed using two well-known isotherms, those of Langmuir and Freundlich. The Langmuir adsorption model assumes that adsorption occurs on a surface with a finite number of sites that are distributed homogeneously on the adsorbent surface. By contrast, the Freundlich adsorption isotherm model assumes a multilayer adsorption of adsorbate molecules on the adsorbent surface, which is heterogeneous and has different energies. The Langmuir isotherm is expressed as follows

$$Q_e = \frac{Q_m K_L C_e}{1 + K_L C_e} \qquad (6)$$

This expression can be further linearized as follows

$$\frac{C_e}{Q_e} = \frac{C_e}{Q_m} + \frac{1}{Q_e K_L} \qquad (7)$$

where Q_m represents the maximum adsorption capacity of the adsorbent ($\text{mg}\cdot\text{g}^{-1}$), K_L ($\text{L}\cdot\text{mg}^{-1}$) is the Langmuir sorption constant at a specific temperature, and C_e is the equilibrium concentration of naphthalene in the solution.

The Langmuir adsorption isotherm was plotted as C_e/Q_e versus C_e, and the values of Q_m and K_L can be calculated using the slope and intercept of the graph (Figure 10a).

The Freundlich isotherm equation and its linearized form are shown in eqs 8 and 9, respectively.

$$Q_e = k_F C_e^{1/n} \qquad (8)$$

$$\ln Q_e = \ln k_F + \frac{1}{n} \ln C_e \qquad (9)$$

where k_F is the Freundlich adsorption constant, which is referred to as the adsorption capacity, and n is the Freundlich constant, which represents the degree of adsorption. The parameters in both isotherm models are summarized in Table 3, along with the values of the linear correlation coefficient.

Table 3. Values of Langmuir and Freundlich Adsorption Isotherm Parameters for the Adsorption of Naphthalene from Wastewater Using the Bi_2MoO_6/rGO (2 wt % rGO) Nanocomposite

adsorption isotherm model	isotherm parameter	value
Langmuir	Q_m, $\text{mg}\cdot\text{g}^{-1}$	173.611
	K_L, $\text{L}\cdot\text{mg}^{-1}$	4.8×10^{-2}
	R^2	0.99
Freundlich	k_F, ($\text{mg}\cdot\text{g}^{-1}$) ($\text{L}\cdot\text{mg}^{-1}$)	1.38097
	$1/n$	1.19
	R^2	0.97

The values of k_F and $1/n$ were calculated using the slope and intercept of the log Q_e versus log C_e plot in Figure 10b. Both models clearly have high R^2 values, although that of the Langmuir adsorption isotherm is slightly higher. The maximum adsorption capacity of naphthalene onto the Bi_2MoO_6/rGO (2 wt % rGO) nanocomposite was determined to be 173.611 $\text{mg}\cdot\text{g}^{-1}$.
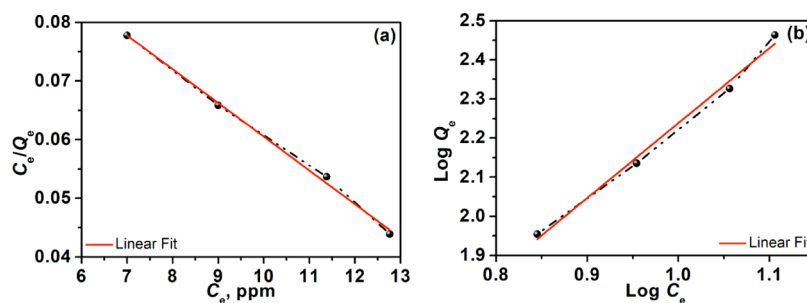
Figure 10. Plots of (a) Langmuir and (b) Freundlich adsorption isotherms for the adsorption of naphthalene from wastewater using the Bi_2MoO_6/rGO (2 wt % rGO) nanocomposite. Red line shows a linear fitting. Conditions: 30 mg of adsorbent [Bi_2MoO_6/rGO (2 wt % rGO) nanocomposite], 100 mL of naphthalene solution, 25 °C, and 60 min.
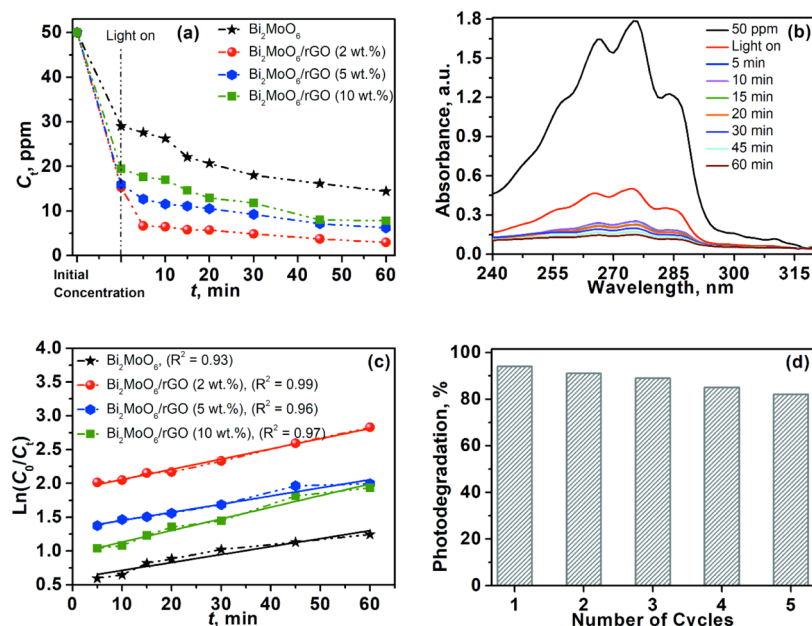
Figure 11. (a) Effect of contact time on the photodegradation of 50 ppm naphthalene under 250 W UV−vis light irradiation using Bi_2MoO_6/rGO nanocomposites. (b) Absorbance intensity of naphthalene at different times during light irradiation for photocatalytic degradation using Bi_2MoO_6/rGO. (c) LH kinetics model of the photocatalytic degradation of naphthalene in solution. (d) Recyclability of the Bi_2MoO_6/rGO (2 wt % rGO) nanocomposite for naphthalene photocatalytic degradation up to five cycles.

2.2.2. Photodegradation Studies.

To investigate the photocatalytic potential of the Bi_2MoO_6/rGO nanocomposite for the degradation of naphthalene in simulated polluted water, 100 mL of a 50 ppm naphthalene aqueous solution and 30 mg of the photocatalyst were mixed and stirred at regular intervals using a magnetic stirrer for 30 min in the absence of light to reach the adsorption−desorption equilibrium. Next, a sample aliquot was extracted. After sampling, the solution was irradiated with UV−vis light (250 W) for 60 min for the photodegradation reaction. Figure 11a shows the photocatalytic efficiency of Bi_2MoO_6 and all the Bi_2MoO_6/rGO nanocomposite samples for the photodegradation of naphthalene in aqueous solution. As in the adsorption process, the naphthalene concentration in the solution decreased as the contact time and exposure to UV−vis light increased until the equilibrium was reached. The photocatalytic efficiency of all the photocatalysts followed the order Bi_2MoO_6 < Bi_2MoO_6/rGO (10 wt % rGO) < Bi_2MoO_6/rGO (5 wt % rGO) < Bi_2MoO_6/rGO (2 wt % rGO). All of the Bi_2MoO_6/rGO nanocomposites exhibited better photocatalytic activity toward naphthalene degradation than Bi_2MoO_6. The effectiveness of the photocatalyst decreased as the rGO content increased, which implies that a high rGO content decreases the number of active sites, resulting in poor photocatalytic degradation. Among the nanocomposites, Bi_2MoO_6/rGO (2 wt % rGO) showed the highest potential for the photocatalytic degradation of naphthalene. Approximately 95% of the naphthalene was successfully degraded using the Bi_2MoO_6/rGO (2 wt % rGO) nanocomposite under visible light irradiation. Figure 11b shows that the absorbance intensity of naphthalene decreases during the photocatalytic degradation using the Bi_2MoO_6/rGO (2 wt % rGO) nanocomposite as a photocatalyst. The intensity decreases with increasing irradiation time. The intensity curves indicate that the photodegradation of naphthalene occurs very rapidly during the first 5 min (>80%) under light irradiation. The rapid decrease in intensity at the beginning of the process

is due to the abundant availability of active sites on the surface of the photocatalyst, which ultimately causes the recombination rate of photogenerated carriers to decrease.

The photocatalytic degradation rate of naphthalene was studied using the Langmuir−Hinshelwood (LH) kinetic model, which is commonly used to elucidate processes with a heterogeneous catalytic rate. The model is expressed as

$$\ln\left(\frac{C_o}{C_t}\right) = k_1 t \tag{10}$$

Here, k_1 is the pseudo-first-order rate constant, which is calculated as follows

$$k_1 = k_T \cdot K \tag{11}$$

Here, k_T is the limiting rate constant of the photocatalytic reaction and K is the adsorption equilibrium constant of the substrate. The plot of ln C_o/C_t versus t (Figure 11c) can be used to determine the value of k_1. It confirms that the LH kinetic model can be applied to the naphthalene photodegradation process. The R^2 values of all the Bi_2MoO_6/rGO nanocomposite photocatalysts are very close to 1, which confirms the suitability of the LH kinetic model for naphthalene photodegradation.

To further examine the performance of the Bi_2MoO_6/rGO nanocomposite, the recyclability and recovery of the photocatalyst were examined. The Bi_2MoO_6/rGO (2 wt % rGO) nanocomposite was recycled after the photodegradation reaction of naphthalene for five cycles. After each cycle, the Bi_2MoO_6/rGO nanocomposite was recovered by centrifugation and purified by washing several times with distilled water. The recovered photocatalyst was then used again for photodegradation reactions under the same reaction conditions. As shown in Figure 11d, the photocatalytic performance was almost unaffected by the recycling cycle, as the efficiency decreased only slightly, from approximately 96% to approximately 82%, after five cycles. Therefore, the photo-

catalyst can be recycled several times and still show good photocatalytic activity. The photocatalyst was used more than four times in this experiment and still showed good photocatalytic results.

The effective potential of the Bi_2MoO_6/rGO nanocomposite compared to pure Bi_2MoO_6 in the photocatalytic degradation of naphthalene can be further explained by photoluminescence (PL) spectroscopy. Figure 12 shows the PL spectra of pure
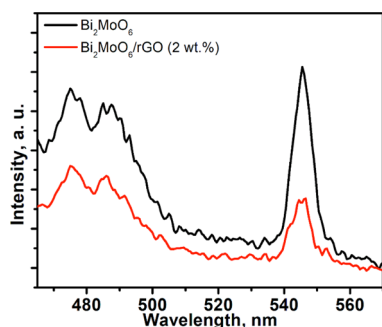
Figure 12. PL spectra of the Bi_2MoO_6 nanostructure and Bi_2MoO_6/rGO (2 wt % rGO) nanocomposite (excitation wavelength = 350 nm).

Bi_2MoO_6 and Bi_2MoO_6/rGO (2 wt % rGO) nanocomposite samples, which were used to investigate the transfer activity of photoexcited charge carriers. The emission spectra of both samples show main peaks centered at 450, 482, and 545 nm, which represent the intrinsic luminescence of Bi_2MoO_6. The fluorescence intensity of the Bi_2MoO_6/rGO (2 wt % rGO) nanocomposite sample is almost half that of pure Bi_2MoO_6. The lower emission intensity of the Bi_2MoO_6/rGO (2 wt % rGO) nanocomposite implies that the incorporation of rGO into the Bi_2MoO_6 matrix decreases the recombination rate of photoexcited electron−hole pairs during transfer, and the rGO can act as an electron acceptor during the photocatalytic process.[46] Therefore, when the Bi_2MoO_6/rGO (2 wt % rGO) nanocomposite is used as a photocatalyst, the recombination rate of photoinduced electrons is lower. As a result, more reactive species are generated during photocatalysis, promoting the separation of electron−hole pairs. The rGO could further facilitate the splitting of electron−hole pairs owing to its conductivity. Thus, the Bi_2MoO_6/rGO (2 wt % rGO) nanocomposite exhibits a stronger photocatalytic activity, and more pollutants can be degraded.

The naphthalene removal mechanism (Figure 13) of the Bi_2MoO_6/rGO nanocomposite can be described as follows. First, naphthalene molecules are adsorbed onto the Bi_2MoO_6/rGO nanocomposite through $\pi-\pi$ interactions between naphthalene and the aromatic rings of rGO. Next, these naphthalene molecules begin to degrade under visible light irradiation. When the Bi_2MoO_6 nanoplates are irradiated, the photogeneration of electrons and holes occurs, generating active superoxide anion radicals and hydroxyl radicals, respectively, and resulting in the photodegradation of naphthalene.[47,48] Therefore, naphthalene is first adsorbed onto the Bi_2MoO_6/rGO nanocomposite from an aqueous solution and degraded into less harmful products through photodegradation.
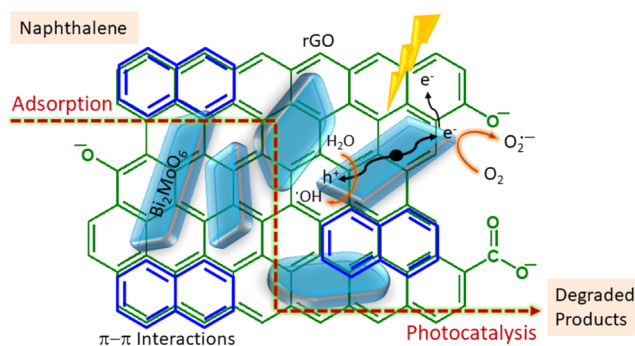
Figure 13. Plausible mechanism for the removal of naphthalene via adsorption−photodegradation.

3. CONCLUSIONS

Heterogeneous photocatalytic materials (Bi_2MoO_6 and Bi_2MoO_6/rGO nanocomposites) were successfully synthesized by a hydrothermal method. These materials were employed for the adsorption-assisted photodegradation of naphthalene (50 ppm) in simulated wastewater. The results revealed that the Bi_2MoO_6/rGO nanocomposite exhibited better adsorption and photocatalytic efficiency than pure Bi_2MoO_6 toward naphthalene degradation in aqueous solution. Bi_2MoO_6 has a narrow band gap, which is sufficient to generate electron−hole pairs under visible light, whereas the fast recombination of charge carriers limits its activity for photocatalysis. The incorporation of rGO into the Bi_2MoO_6/rGO nanocomposite played a significant role in improving the adsorption and photocatalytic efficiency of the nanocomposite material. The rGO in the nanocomposite improved the adsorption of naphthalene molecules onto the surface of the photocatalyst through $\pi-\pi$ interactions, resulting in successful naphthalene degradation. Naphthalene adsorption followed the Langmuir adsorption and pseudo-second-order kinetics. Furthermore, rGO acted as an electron sink and suppressed the recombination of photogenerated charge carriers and thus promoted the photocatalytic efficiency of the material. Among the Bi_2MoO_6/rGO nanocomposites, the Bi_2MoO_6/rGO (2 wt % rGO) material exhibited better photodegradation efficiency, possibly owing to its large active surface area, efficient electron transfer, and lower electron−hole recombination rate. Approximately 95% of naphthalene was degraded during 60 min of visible light irradiation using Bi_2MoO_6/rGO (2 wt % rGO). The photocatalyst was successfully recovered through centrifugation and successfully recycled. The remarkable performance of Bi_2MoO_6/rGO in this study suggests a clean and sustainable approach to the remediation of wastewater.

4. EXPERIMENTAL SECTION

4.1. Materials. Bismuth(III) nitrate pentahydrate [Bi(NO$_3$)$_3$·5H$_2$O, 98%], sodium molybdate dehydrate (Na$_2$MoO$_4$·2H$_2$O, 99%), and ethylene glycol (99%) were purchased from Sigma-Aldrich and were used together with ethanol (99%) obtained from Minema Chemicals (Johannesburg) for the synthesis of Bi_2MoO_6. GO was synthesized using H$_2$O$_2$, HCl, H$_2$SO$_4$/H$_3$PO$_4$, KMnO$_4$, and graphite powder. The naphthalene flakes used to prepare PAH-contaminated water were purchased from Associated Chemical Enterprises, Johannesburg. Deionized water was used in all the experiments. All chemicals were analytically pure and were used with no further purification.

4.2. Synthesis of Bi$_2$MoO$_6$. Bi$_2$MoO$_6$ was prepared by mixing the Bi and Mo precursors at 25 °C. Bi(NO$_3$)$_3$·5H$_2$O (1.212 g) was used as the Bi precursor and dissolved in ethylene glycol (5 mL), whereas the Mo precursor, Na$_2$MoO$_4$·2H$_2$O (0.030 g), was dissolved in ethanol (30 mL). Both solutions were then mixed at 25 °C for 30 min until a brownish solution appeared. The obtained solution was transferred to a Teflon-lined stainless steel hydrothermal autoclave for hydrothermal treatment at 180 °C for 16 h. The solution in the autoclave was then allowed to cool down naturally. After the hydrothermal treatment, the obtained precipitate was collected from the solution by centrifugation. To remove impurities, the precipitate was washed thoroughly several times using deionized water with centrifugation and dried in a vacuum oven for 24 h at 60 °C.

4.3. Synthesis of GO. GO was synthesized according to the improved Hummers method. In a typical procedure, 3.0 g of commercially available graphite powder was added to a concentrated 400 mL H$_2$SO$_4$/H$_3$PO$_4$ (9:1) solution. KMnO$_4$ (18.0 g) was added slowly, and the mixture was stirred continuously for 12 h.[49] Because the reaction is exothermic, the reaction mixture produces some heat, and the reaction temperature was maintained at 50 °C. Next, the reaction mixture was allowed to cool down naturally and charged with ice (500 mL) and 3 mL of 30% H$_2$O$_2$. The oxidized GO was collected by centrifugation, and the supernatant was decanted. The solid brown precipitate was washed several times with deionized water, 10% HCl, and finally ethanol. The obtained brown GO was exfoliated to a few GO layers through ultrasonication in water. A GO solution in an aqueous medium was employed to prepare Bi$_2$MoO$_6$/rGO.

4.4. Synthesis of Bi$_2$MoO$_6$/rGO Nanocomposites. Several Bi$_2$MoO$_6$/rGO nanocomposites were prepared using different amounts of GO (2, 5, and 10 wt %) with Bi$_2$MoO$_6$. A typical synthesis procedure for Bi$_2$MoO$_6$/rGO (containing 10 wt % rGO) was as follows: 0.7272 g of Bi (NO$_3$)$_3$·5H$_2$O was dissolved in 5 mL of ethylene glycol, and 40 mg of GO in water dispersion was added. The reaction mixture was stirred for 10 min at 25 °C. Subsequently, 0.1812 g of Na$_2$MoO$_4$·2H$_2$O was dissolved in 30 mL of ethanol and added to the above solution, which was further stirred for 30 min. The prepared mixture was poured into the Teflon-lined stainless steel hydrothermal autoclave for hydrothermal treatment at 180 °C for 16 h. The resulting sample was cooled naturally and then washed and dried following the procedure used for the Bi$_2$MoO$_6$ sample. During the synthesis of the Bi$_2$MoO$_6$/rGO nanocomposite, GO was hydrothermally reduced to rGO in situ at 180 °C.[32] Other samples were prepared following the same route using 20 or 8 mg of GO to obtain the Bi$_2$MoO$_6$/rGO (5 wt %) and Bi$_2$MoO$_6$/rGO (2 wt %) nanocomposites, respectively.

4.5. Characterization Techniques. XRD analysis was used to determine the crystallinity, purity, and phase of the synthesized samples. The XRD patterns were obtained using a Philips Analytical X'Pert PRO PW 3050/60 at a voltage of 40 kV with Cu Kα radiation in the diffraction angle (2θ) range of 5−90°. FTIR spectra were acquired in the range of 400−4000 cm^{-1} using a PerkinElmer Spectrum 100 FTIR spectrophotometer with KBr pellets. The morphology and structural features of the synthesized materials were investigated using FESEM (Zeiss Auriga). The characteristic elemental distributions of the samples were analyzed using an EDX spectrometer (Oxford, UK) coupled with FESEM. The size and structure of

the samples were further investigated using HRTEM (JEOL JEM-2100). To investigate the chemical composition, oxidation state, and binding energy of each element in the nanocomposite material, XPS measurements were performed using an Axis Ultra device (Kratos, UK) with a monochromatic (Al Kα) excitation source. The background XPS spectrum of each material was corrected using Shirley background correction, and all the recorded XPS peaks were constructed using Gaussian functions. The specific surface area and porosity of the samples were recorded on a Micromeritics (ASAP 2020, USA) analyzer using nitrogen adsorption−desorption isotherms. UV−vis absorbance analysis was performed using a LAMBDA 750 UV−vis−NIR spectrophotometer (PerkinElmer, USA). PL spectroscopy was conducted on a Horiba Jobin−Yvon NanoLog spectrometer under excitation by a Xe lamp at 325 nm.

4.6. Adsorption and Photodegradation Experiments. The photocatalytic potentials of the prepared Bi$_2$MoO$_6$ and Bi$_2$MoO$_6$/rGO nanocomposites were assessed by measuring the degradation of naphthalene in an aqueous solution under visible light. Naphthalene was used as a model PAH water contaminant. Simulated wastewater was prepared by dissolving naphthalene flakes in a 10% methanol aqueous solution at 25 °C. In each test, 30 mg of the photocatalyst was completely suspended in 100 mL of the simulated naphthalene-contaminated (50 ppm) wastewater. Before exposure to the UV−vis light, the solution was magnetically agitated in the dark for 30 min to establish the adsorption−desorption equilibrium between naphthalene and the surface of the photocatalyst. Approximately 5 mL of the reaction solution was extracted before the light was turned on to initiate the photocatalytic degradation of naphthalene in the water. Then, the simulated naphthalene-contaminated wastewater was exposed to visible light for 60 min. At 5, 10, 15, 20, 30, 45, and 60 min, an aliquot of approximately 5 mL of the reaction solution was removed. To ensure that the collected reaction solution did not contain the catalyst, the sample aliquot was passed through a syringe filter (0.45 μm). The naphthalene concentration of the collected samples after photodegradation was analyzed using a LAMBDA 750S UV−vis spectrophotometer (PerkinElmer) at wavelengths of 200−500 nm, where distilled water was used as the background. The intensity at 275 nm of the UV−vis diffuse spectra indicated the amount of naphthalene remaining in the wastewater. To evaluate the adsorption ability of the prepared photocatalyst, another reaction was performed in the dark for 60 min, and the solution was sampled at the time intervals mentioned above. All the collected samples were analyzed using a UV−vis spectrometer. In this process, 30 mg of the Bi$_2$MoO$_6$/rGO (2 wt % rGO) nanocomposite was added to 100 mL of naphthalene aqueous solution with a concentration of 50 ppm under dark conditions.

■ AUTHOR INFORMATION

Corresponding Authors

Elvis Fosso-Kankeu − *Water Pollution Monitoring and Remediation Initiatives Research Group, School of Chemical and Minerals Engineering, North West University, Potchefstroom 2520, South Africa*; Email: elvisfosso.ef@gmail.com, Elvis.FossoKankeu@nwu.ac.za

Suprakas Sinha Ray − *Centre for Nanostructures and Advanced Materials, DSI-CSIR Nanotechnology Innovation Centre, Council for Scientific and Industrial Research,*

Pretoria 0001, South Africa; Department of Chemical Sciences, University of Johannesburg, Johannesburg 2028, South Africa; ● orcid.org/0000-0002-0007-2595; Email: rsuprakas@csir.co.za, ssinharay@uj.ac.za

Authors

Shelter Maswanganyi − Water Pollution Monitoring and Remediation Initiatives Research Group, School of Chemical and Minerals Engineering, North West University, Potchefstroom 2520, South Africa

Rashi Gusain − Centre for Nanostructures and Advanced Materials, DSI-CSIR Nanotechnology Innovation Centre, Council for Scientific and Industrial Research, Pretoria 0001, South Africa; Department of Chemical Sciences, University of Johannesburg, Johannesburg 2028, South Africa

Neeraj Kumar − Centre for Nanostructures and Advanced Materials, DSI-CSIR Nanotechnology Innovation Centre, Council for Scientific and Industrial Research, Pretoria 0001, South Africa; ● orcid.org/0000-0001-5019-6329

Frans Boudewijn Waanders − Water Pollution Monitoring and Remediation Initiatives Research Group, School of Chemical and Minerals Engineering, North West University, Potchefstroom 2520, South Africa

Complete contact information is available at:
https://pubs.acs.org/10.1021/acsomega.1c01296

Notes

The authors declare no competing financial interest.

■ REFERENCES

(1) Kabra, K.; Chaudhary, R.; Sawhney, R. L. Treatment of hazardous organic and inorganic compounds through aqueous-phase photocatalysis: A review. Ind. Eng. Chem. Res. 2004, 43, 7683−7696.

(2) Quesada, H. B.; Baptista, A. T. A.; Cusioli, L. F.; Seibert, D.; de Oliveira Bezerra, C.; Bergamasco, R. Surface water pollution by pharmaceuticals and an alternative of removal by low-cost adsorbents: A review. Chemosphere 2019, 222, 766−780.

(3) Gusain, R.; Kumar, N.; Ray, S. S. Recent advances in carbon nanomaterial-based adsorbents for water purification. Coord. Chem. Rev. 2020, 405, 213111.

(4) Ray, S. S.; Gusain, R.; Kumar, N. Carbon Nanomaterial-Based Adsorbents for Water Purification: Fundamentals and Applications; Elsevier, 2020.

(5) Ama, O. M.; Kumar, N.; Adams, F. V.; Ray, S. S. Efficient and cost-effective photoelectrochemical degradation of dyes in wastewater over an exfoliated graphite-MoO 3 nanocomposite electrode. Electrocatalysis 2018, 9, 623−631.

(6) Abdel-Shafy, H. I.; Mansour, M. S. M. A review on polycyclic aromatic hydrocarbons: Source, environmental impact, effect on human health and remediation. Egypt. J. Pet. 2016, 25, 107−123.

(7) Mojiri, A.; Zhou, J. L.; Ohashi, A.; Ozaki, N.; Kindaichi, T. Comprehensive review of polycyclic aromatic hydrocarbons in water sources, their effects and treatments. Sci. Total Environ. 2019, 696, 133971.

(8) Walaszek, M.; Bois, P.; Laurent, J.; Lenormand, E.; Wanko, A. Micropollutants removal and storage efficiencies in urban stormwater constructed wetland. Sci. Total Environ. 2018, 645, 854−864.

(9) García-Martínez, M. J.; Ortega, M. F.; Bolonio, D.; Llamas, J. F.; Canoira, L. Leaching of polycyclic aromatic hydrocarbons (PAHs) from coal dumps reclaimed with apple trees: a mechanistic insight. Environ. Geochem. Health 2018, 40, 2695−2706.

(10) Rengarajan, T.; Rajendran, P.; Nandakumar, N.; Lokeshkumar, B.; Rajendran, P.; Nishigaki, I. Exposure to polycyclic aromatic hydrocarbons with special focus on cancer. Asian Pac. J. Trop. Biomed. 2015, 5, 182−189.

(11) Adeola, A. O.; Forbes, P. B. C. Advances in water treatment technologies for removal of polycyclic aromatic hydrocarbons: Existing concepts, emerging trends, and future prospects. Water Environ. Res. 2021, 93, 343−359.

(12) Lamichhane, S.; Bal Krishna, K. C.; Sarukkalige, R. Polycyclic aromatic hydrocarbons (PAHs) removal by sorption: A review. Chemosphere 2016, 148, 336−353.

(13) Zeng, Y.; Hong, P. A.; Wavrek, D. A. Chemical−biological treatment of pyrene. Water Res. 2000, 34, 1157−1172.

(14) Zheng, X.-J.; Blais, J.-F.; Mercier, G.; Bergeron, M.; Drogui, P. PAH removal from spiked municipal wastewater sewage sludge using biological, chemical and electrochemical treatments. Chemosphere 2007, 68, 1143−1152.

(15) Oturan, M. A.; Aaron, J.-J. Advanced oxidation processes in water/wastewater treatment: principles and applications. A review. Crit. Rev. Environ. Sci. Technol. 2014, 44, 2577−2641.

(16) Mukwevho, N.; Kumar, N.; Fosso-Kankeu, E.; Waanders, F.; Bunt, J.; Ray, S. S. Visible light-excitable ZnO/2D graphitic-C_3N_4 heterostructure for the photodegradation of naphthalene. Desalin. Water Treat. 2019, 163, 286−296.

(17) Mukwevho, N.; Fosso-Kankeu, E.; Waanders, F.; Kumar, N.; Ray, S. S.; Yangkou Mbianda, X. Photocatalytic activity of $Gd_2O_2CO_3$· ZnO·CuO nanocomposite used for the degradation of phenanthrene. SN Appl. Sci. 2019, 1, 10.

(18) García-Martínez, M. J.; Da Riva, I.; Canoira, L.; Llamas, J. F.; Alcántara, R.; Gallego, J. L. R. Photodegradation of polycyclic aromatic hydrocarbons in fossil fuels catalysed by supported TiO_2. Appl. Catal., B 2006, 67, 279−289.

(19) Nguyen, V.-H.; Phan Thi, L.-A.; Van Le, Q.; Singh, P.; Raizada, P.; Kajitvichyanukul, P. Tailored photocatalysts and revealed reaction pathways for photodegradation of polycyclic aromatic hydrocarbons (PAHs) in water, soil and other sources. Chemosphere 2020, 260, 127529.

(20) Guo, J.; Shi, L.; Zhao, J.; Wang, Y.; Tang, K.; Zhang, W.; Xie, C.; Yuan, X. Enhanced visible-light photocatalytic activity of Bi2MoO6 nanoplates with heterogeneous Bi2MoO6-x@Bi2MoO6 core-shell structure. Appl. Catal., B 2018, 224, 692−704.

(21) Wang, Y.; Niu, C.-G.; Zhang, L.; Wang, Y.; Zhang, H.; Huang, D.-W.; Zhang, X.-G.; Wang, L.; Zeng, G.-M. High-efficiency visible-light AgI/Ag/Bi_2MoO_6 as a Z-scheme photocatalyst for environmental applications. RSC Adv. 2016, 6, 10221−10228.

(22) Zhang, J.; Niu, C.; Ke, J.; Zhou, L.; Zeng, G. Ag/AgCl/ Bi_2MoO_6 composite nanosheets: A plasmonic Z-scheme visible light photocatalyst. Catal. Commun. 2015, 59, 30−34.

(23) Ding, J.; Yang, Z.; He, C.; Tong, X.; Li, Y.; Niu, X.; Zhang, H. UiO-66 (Zr) coupled with Bi2MoO6 as photocatalyst for visible-light promoted dye degradation. J. Colloid Interface Sci. 2017, 497, 126−133.

(24) Martínez-de la Cruz, A.; Obregón Alfaro, S. Synthesis and characterization of γ-Bi2MoO6 prepared by co-precipitation: photo-assisted degradation of organic dyes under vis-irradiation. J. Mol. Catal. A: Chem. 2010, 320, 85−91.

(25) Mungse, H. P.; Verma, S.; Kumar, N.; Sain, B.; Khatri, O. P. Grafting of oxo-vanadium Schiff base on graphene nanosheets and its catalytic activity for the oxidation of alcohols. J. Mater. Chem. 2012, 22, 5427−5433.

(26) Uma, K.; Chong, S.; Mohan, S. C.; Jothivenkatachalam, K.; Yang, T. C.-K.; Lin, J.-H. Multi-functional RGO-supported α-Fe2O3 nanocomposites for high-performance pseudocapacitors and visible light−driven photocatalytic applications. Ionics 2020, 26, 3491−3500.

(27) Xie, S.; Liu, Y.; Deng, J.; Yang, J.; Zhao, X.; Han, Z.; Zhang, K.; Lu, Y.; Liu, F.; Dai, H. Carbon monoxide oxidation over rGO-mediated gold/cobalt oxide catalysts with strong metal−support interaction. *ACS Appl. Mater. Interfaces* **2020**, *12*, 31467−31476.

(28) Zhao, J.; Yang, Y.; Yu, W.; Ma, Q.; Dong, X.; Wang, X.; Wang, J.; Liu, G. Bi_2MoO_6/RGO composite nanofibers: facile electrospinning fabrication, structure, and significantly improved photocatalytic water splitting activity. *J. Mater. Sci.: Mater. Electron.* **2017**, *28*, 543−552.

(29) Dai, W.; Xiong, W.; Yu, J.; Zhang, S.; Li, B.; Yang, L.; Wang, T.; Luo, X.; Zou, J.; Luo, S. Bi_2MoO_6 Quantum dots in situ grown on reduced graphene oxide layers: A novel electron-rich interface for efficient CO_2 reduction. *ACS Appl. Mater. Interfaces* **2020**, *12*, 25861−25874.

(30) Kasinathan, M.; Thiripuranthagan, S.; Sivakumar, A.; Ranganathan, S.; Vembuli, T.; Kumaravel, S.; Erusappan, E. Fabrication of novel Bi_2MoO_6/N-rGO catalyst for the efficient photocatalytic degradation of harmful dyes. *Mater. Res. Bull.* **2020**, *125*, 110782.

(31) Hao, Y.; Dong, X.; Wang, X.; Zhai, S.; Ma, H.; Zhang, X. Controllable electrostatic self-assembly of sub-3 nm graphene quantum dots incorporated into mesoporous Bi2MoO6 frameworks: efficient physical and chemical simultaneous co-catalysis for photocatalytic oxidation. *J. Mater. Chem. A* **2016**, *4*, 8298−8307.

(32) Kumar, N.; Salehiyan, R.; Chauke, V.; Joseph Botlhoko, O.; Setshedi, K.; Scriba, M.; Masukume, M.; Sinha Ray, S. Top-down synthesis of graphene: A comprehensive review. *FlatChem* **2021**, *27*, 100224.

(33) Zhang, L.; Xu, T.; Zhao, X.; Zhu, Y. Controllable synthesis of Bi_2MoO_6 and effect of morphology and variation in local structure on photocatalytic activities. *Appl. Catal., B* **2010**, *98*, 138−146.

(34) Zhang, J.; Liu, Z.; Ma, Z. Facile Formation of Bi2O2CO3/Bi2MoO6 Nanosheets for Visible Light-Driven Photocatalysis. *ACS Omega* **2019**, *4*, 3871−3880.

(35) Wan, S.; Ou, M.; Zhong, Q.; Zhang, S.; Song, F. Construction of Z-scheme photocatalytic systems using $ZnIn_2S_4$, CoO_x-loaded Bi_2MoO_6 and reduced graphene oxide electron mediator and its efficient nonsacrificial water splitting under visible light. *Chem. Eng. J.* **2017**, *325*, 690−699.

(36) Sindhu, S.; Sanghi, S.; Agarwal, A.; Seth, V. P.; Kishore, N. Effect of Bi_2O_3 content on the optical band gap, density and electrical conductivity of $MO \cdot Bi_2O_3 \cdot B_2O_3$ (M= Ba, Sr) glasses. *Mater. Chem. Phys.* **2005**, *90*, 83−89.

(37) Xiao, J.; Zhang, J.; Liu, W.; Huang, T.; Qu, Y.; Chen, H.; Lin, Z. Construction of rGO/Bi2MoO6 2D/2D nanocomposites for enhancement visible light-driven photocatalytic reduction of Cr (VI). *Mater. Res. Express* **2018**, *5*, 115031.

(38) Kumar, N.; Mittal, H.; Parashar, V.; Ray, S. S.; Ngila, J. C. Efficient removal of rhodamine 6G dye from aqueous solution using nickel sulphide incorporated polyacrylamide grafted gum karaya bionanocomposite hydrogel. *RSC Adv.* **2016**, *6*, 21929−21939.

(39) Kumar, N.; Mittal, H.; Alhassan, S. M.; Ray, S. S. Bionanocomposite hydrogel for the adsorption of dye and reusability of generated waste for the photodegradation of ciprofloxacin: A demonstration of the circularity concept for water purification. *ACS Sustainable Chem. Eng.* **2018**, *6*, 17011−17025.

(40) Zhao, J.; Lu, Q.; Wei, M.; Wang, C. Synthesis of one-dimensional $α$-Fe2O3/Bi2MoO6 heterostructures by electrospinning process with enhanced photocatalytic activity. *J. Alloys Compd.* **2015**, *646*, 417−424.

(41) Liu, Y.; Yang, Z.-H.; Song, P.-P.; Xu, R.; Wang, H. Facile synthesis of Bi2MoO6/ZnSnO3 heterojunction with enhanced visible light photocatalytic degradation of methylene blue. *Appl. Surf. Sci.* **2018**, *430*, 561−570.

(42) Kumar, N.; Fosso-Kankeu, E.; Ray, S. S. Achieving controllable MoS_2 nanostructures with increased interlayer spacing for efficient removal of Pb(II) from aquatic systems. *ACS Appl. Mater. Interfaces* **2019**, *11*, 19141−19155.

(43) Sharma, M.; Behl, K.; Nigam, S.; Joshi, M. TiO_2-GO nanocomposite for photocatalysis and environmental applications: A green synthesis approach. *Vacuum* **2018**, *156*, 434−439.

(44) Donohue, M. D.; Aranovich, G. L. Classification of Gibbs adsorption isotherms. *Adv. Colloid Interface Sci.* **1998**, *76*, 137−152.

(45) Mukwevho, N.; Gusain, R.; Fosso-Kankeu, E.; Kumar, N.; Waanders, F.; Ray, S. S. Removal of naphthalene from simulated wastewater through adsorption-photodegradation by ZnO/Ag/GO nanocomposite. *J. Ind. Eng. Chem.* **2020**, *81*, 393−404.

(46) Yang, J.; Wang, X.; Zhao, X.; Dai, J.; Mo, S. Synthesis of uniform Bi_2WO_6-reduced graphene oxide nanocomposites with significantly enhanced photocatalytic reduction activity. *J. Phys. Chem. C* **2015**, *119*, 3068−3078.

(47) Kumar, N.; Sinha Ray, S.; Ngila, J. C. Ionic liquid-assisted synthesis of Ag/Ag_2Te nanocrystals via a hydrothermal route for enhanced photocatalytic performance. *New J. Chem.* **2017**, *41*, 14618−14626.

(48) Byrne, C.; Subramanian, G.; Pillai, S. C. Recent advances in photocatalysis for environmental applications. *J. Environ. Chem. Eng.* **2018**, *6*, 3531−3555.

(49) Kumar, N.; Kumar, S.; Gusain, R.; Manyala, N.; Eslava, S.; Ray, S. S. Polypyrrole-promoted rGO−MoS_2 Nanocomposites for Enhanced Photocatalytic Conversion of CO_2 and H_2O to CO, CH_4, and H_2 Products. *ACS Appl. Energy Mater.* **2020**, *3*, 9897−9909.